The Fate of ZnO Nanoparticles Administered to Human Bronchial Epithelial Cells

Benjamin Gilbert,[†,#,*] Sirine C. Fakra,[‡,#] Tian Xia,[§,#] Suman Pokhrel,[¶] Lutz Mädler,[¶] and André E. Nel[§,*]

[†]Earth Sciences Division and [‡]Advanced Light Source, Lawrence Berkeley National Laboratory, Berkeley, California, United States, [§]Department of Medicine—Division of NanoMedicine, University of California, Los Angeles, California, United States, and [¶]Foundation Institute of Materials Science (IWT), Department of Production Engineering, University of Bremen, Germany. [#]These authors contributed equally.

The development of nanoscale materials with physical or chemical properties that are modified or enhanced relative to their bulk counterparts continues to offer enormous possibilities for novel applications in research, technology, and industry. However, several properties of nanomaterials justify particular cause for concern as to their biological interactions and human health impacts. Individual studies have shown that nanomaterials may be transported within organisms and into cells and exert toxic effects through unconventional mechanisms (see Table 2 in Nel et al.[1]). At present, a full description of the environmental fate and human toxicity of even the most common nanomaterials remains to be achieved. Zinc oxide (ZnO) is an important example because it is now widely used as a nanocrystalline additive to sunscreen,[2] with further anticipated applications such as photovoltaic devices and nanomechanical components.[3−5] ZnO nanomaterials have proven toxicity in human and other mammalian cell lines[6−9] and in soil and aquatic organisms that are indicator species for ecosystem health,[10−16] but the mechanism of toxicity is not clearly established.

ZnO nanomaterials represent an important class of toxicant because ZnO is unstable in aqueous solutions, dissolving to release Zn^{2+}, a physiologically essential metal ion that is itself toxic at elevated levels.[17,18] Other oxide nanomaterials including copper oxide exhibit similar behavior.[14,19,20] The tendency of ZnO nanoparticles to dissolve in aqueous solutions, especially biological fluids, has been well documented,[12,21,22] but the relative contributions of nanoparticulate and dissolved zinc to the uptake, subcellular localization, and mechanism(s) of toxicity remain very challenging to assess directly. In prior work, we combined cellular

ABSTRACT
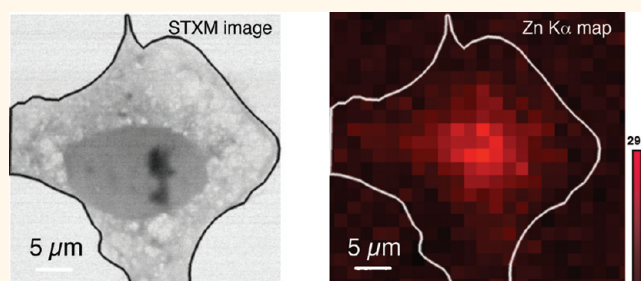
A particular challenge for nanotoxicology is the evaluation of the biological fate and toxicity of nanomaterials that dissolve in aqueous fluids. Zinc oxide nanomaterials are of particular concern because dissolution leads to release of the toxic divalent zinc ion. Although zinc ions have been implicated in ZnO cytotoxicity, direct identification of the chemical form of zinc taken up by cells exposed to ZnO nanoparticles, and its intracellular fate, has not yet been achieved. We combined high resolution X-ray spectromicroscopy and high elemental sensitivity X-ray microprobe analyses to determine the fate of ZnO and less soluble iron-doped ZnO nanoparticles following exposure to cultures of human bronchial epithelial cells, BEAS-2B. We complemented two-dimensional X-ray imaging methods with atomic force microscopy of cell surfaces to distinguish between nanoparticles that were transported inside the cells from those that adhered to the cell exterior. The data suggest cellular uptake of ZnO nanoparticles is a mechanism of zinc accumulation in cells. Following uptake, ZnO nanoparticles dissolved completely generating intracellular Zn^{2+} complexed by molecular ligands. These results corroborate a model for ZnO nanoparticle toxicity that is based on nanoparticle uptake followed by intracellular dissolution.

KEYWORDS: nanotoxicology · ZnO cytotoxicity · cellular uptake · X-ray spectromicroscopy

toxicity assays, optical and electron microscopy, and abiotic nanoparticle dissolution studies to assess ZnO toxicity to cultured human macrophages and epithelial cells.[17,18] The data were consistent with a model for toxicity based on a mechanism of nanoparticle uptake followed by intracellular dissolution and Zn^{2+} release. Zn release could induce oxidative stress inside cells that leads to cell death.[17,23] This model was

further substantiated by the design and synthesis of ZnO nanoparticles that were doped with iron to reduce their solubility, a modification leading to reduced toxicity.[18,24] However, direct identification of the chemical form of zinc taken up by cells exposed to ZnO nanoparticles, and its intracellular fate, has not yet been achieved.

Conventional methods capable of imaging nano-materials in organisms and cells have not been successful at directly establishing the fate of ZnO nanoparticles administered to cell cultures. Optical fluorescence microscopy and transmission electron microscopy have both been used to demonstrate the uptake and accumulation of quantum dots and labeled nanoma-terials by cultured cells.[25] These approaches were successful for localizing aggregates and individual nanoparticles of TiO_2, CeO_2, and other nanoparticles in human macrophage and lung cells, but were never successful at locating intracellular ZnO nanoparticles. The failure of conventional imaging techniques is likely a consequence of complete or partial ZnO dissolution, and consequently a detailed model of zinc uptake has not been confidently established.

Synchrotron-based X-ray techniques offer alterna-tive approaches for mapping the distribution and speciation of zinc in cells and organisms. We used X-ray fluorescence (XRF) microprobe and scanning transmission X-ray microscopy (STXM) to address the fate of zinc following the exposure of ZnO nanoparti-cles to human cell cultures. We used microfocused XRF elemental mapping to obtain the distribution of zinc in cells and used micro-X-ray absorption near-edge struc-ture (XANES) spectroscopy to investigate the chemical speciation of intracellular zinc. Hard-X-ray microprobes have been successfully used for example to spatially localize physiological zinc in tissues,[26] to map the bio-accumulation of zinc following the administration of ZnO nanoparticles to the velvet mesquite plant,[27] and to determine zinc speciation in contaminated soils.[28]

Cultured cells were also examined at higher spatial resolution (~30 nm) using STXM at the Zn $L_{2,3}$ and Fe $L_{2,3}$ edges. While several groups have performed STXM imaging of eukaryotic cells,[29−32] there are very few STXM studies to date of cultured mammalian cells. Recently, Graf et al. demonstrated STXM imaging of 160-nm gold-coated silica nanoparticles within ultra-sectioned skin tissue.[33] So far, STXM has been widely used to study polymers and chemical interactions between bacteria, extracellular organic molecules, and nanoscale minerals in heterogeneous environmental systems.[34,35]

Hard X-ray fluorescence microprobe instruments typically have a lower detection limit than soft X-ray STXM, proton impact X-ray emission (PIXE) and energy dispersive X-ray (EDX) spectrometry but are generally limited in spatial resolution. The optimal spatial resolu-tion at the beamline we used is 2 μm × 2 μm. We
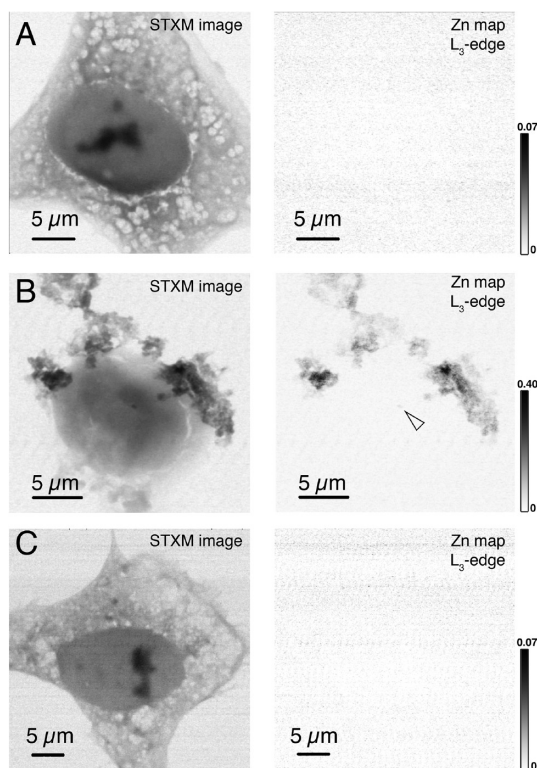

Figure 1. Scanning transmission X-ray microscopy (STXM) analysis of one control culture of BEAS-2B cells and two BEAS-2B cell cultures exposed to BSA-coated ZnO nanopar-ticles at 50 μg/mL for 1 h. (A) STXM image and correspond-ing Zn map of a cell from the control. (B) STXM image and corresponding Zn map of a cell from a sample that received a mild washing treatment following ZnO exposure. The smallest detected zinc-rich object is indicated by the arrow. (C) STXM image and corresponding Zn map of a cell from a sample that was washed vigorously following ZnO expo-sure. STXM images were acquired at 1028 eV and Zn distribution maps were derived from X-ray images recorded at 1015 and 1028 eV.

estimated from measurements on a XRF Zn calibration standard a detection limit for Zn at around 0.05 μg/cm^2, equivalent to a concentration in a 1-μm thick sample of 1.5 μM. The soft X-ray STXM we used has an optimum spatial resolution of 10 nm. The STXM detection limit for zinc is affected by many factors, and has not been measured, but it is at least an order of magnitude greater than the hard X-ray microprobe.

Because a major conclusion of prior work is that ZnO nanoparticles are taken up by cells prior to dissolution, the goals of this research were to map the intracellular zinc and determine whether solid phase nanomater-ials, dissolved zinc, or a mixture, were present inside the cells following exposure. Although STXM and μXRF analyses of hydrated cells are possible, we chose to fix and dehydrate the samples at a single time point following exposure. Fixation stabilized cell morphol-ogy and chemistry, permitting complementary studies to be performed sequentially on the same cells while minimizing sample change between analyses. Because no single approach was able to reveal all aspects of the
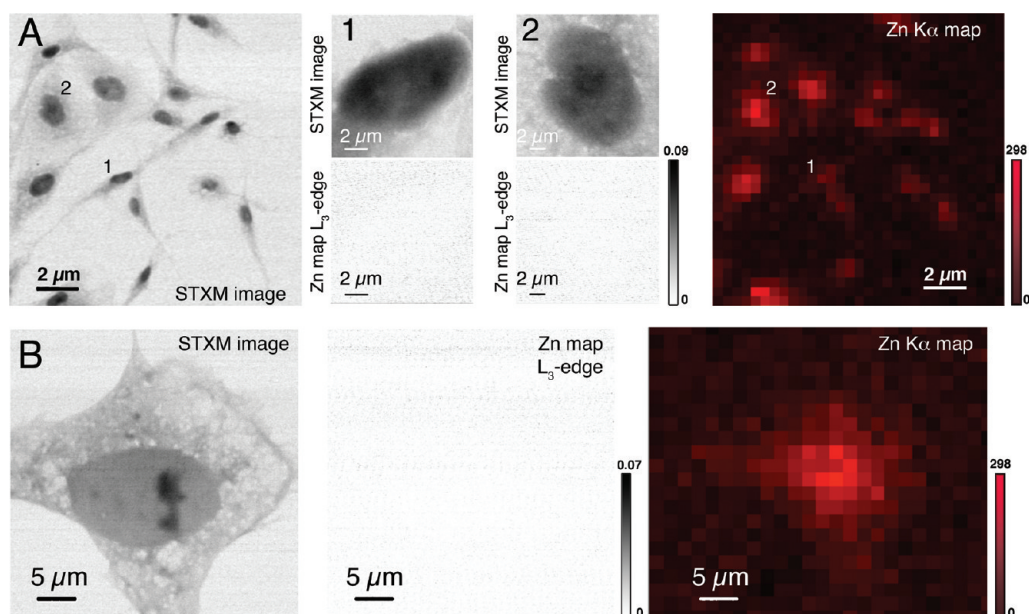
Figure 2. Scanning transmission X-ray microscopy (STXM; gray images) and micro-X-ray fluorescence (μXRF; red images) mapping of intracellular zinc within BEAS-2B cells exposed to (A) 600 μM ZnSO$_4$ or (B) BSA-coated ZnO nanoparticles. Individual cells are clearly imaged by STXM at 30-nm resolution but intracellular zinc is undetectable at the Zn L$_3$-edge. By contrast, μXRF elemental mapping performed on the same cells show zinc-rich areas. XRF maps were recorded at 11 keV, using a 6 μm × 6 μm beam spot size and 3 μm × 3 μm pixel size. As shown in Figure 3 and Supporting Information, Figure S2, a low background concentration of physiological zinc was detected from the control sample.

zinc distribution and chemistry, the use of multiple methods was essential to correlate the distribution of nanoparticulate *versus* free zinc within cells and to distinguish internalized and surface-bound nanoparticle aggregates.

RESULTS

X-ray Spectromicroscopy Studies of Control Cells and Cells Exposed to ZnO Nanoparticles. A representative STXM image of a portion of a BEAS-2B cell from a control culture is given in Figure 1A, recorded at 1015 eV, just below the Zn L$_3$ absorption edge. Below the edge, the image contrast derives primarily from X-ray attenuation which is proportional to mass density and energy.[29] Cell nuclei appear as higher-density regions than cytoplasm, and occasionally feature denser intranuclear domains (nucleoli), previously observed in X-ray microscopy studies of fibroblast cells.[30]

The effectiveness of the sample preparation procedures for removing excess ZnO following exposure was evaluated with STXM imaging of BEAS-2B cells exposed to undoped ZnO nanoparticles, as shown in Figure 1B. When the cells were not vigorously washed following nanoparticle exposure, large nanoparticle aggregates were often found associated with cell surfaces. In contrast, ZnO nanoparticle aggregates were almost never observed on properly washed samples. The clean cell shown in Figure 1C is typical of vigorously washed samples, and all further samples received this treatment.

We performed STXM and microprobe analyses of BEAS-2B cells that were grown under control (zinc-free)

conditions or that were exposed to growth medium containing ZnO nanoparticles or dissolved Zn^{2+} from soluble zinc sulfate. We used a ZnO concentration of 50 μg/mL (625 μM Zn), previously shown to induce multiple stages of the hierarchical oxidative stress response without cell death within one hour of exposure.[17] Although ZnO nanoparticles start to dissolve immediately upon addition to BGEM, abiotic experiments showed that the maximum Zn^{2+}(aq) concentration attained within 4 days never exceeded 223 μM, indicating that the majority of the administered ZnO does not dissolve in the growth medium.

We sought to map the intracellular distribution of zinc within control cells and cells exposed to ZnO or Zn^{2+}(aq) using STXM at the Zn L$_{2,3}$-edge. Zinc was not detected in any cell or substrate region, either as discrete solid-phase nanoparticles or aggregates, or as diffuse signal (Figure 2). By contrast, when a cell culture was exposed to growth medium containing insoluble TiO$_2$ nanoparticles at 50 μg/mL, STXM imaging at the Ti L$_3$-edge revealed Ti-rich cell-associated nanoparticle aggregates (Supporting Information, Figure S1), in agreement with prior TEM studies (see supplemental data to ref 17). We also exposed one cell culture to a four times higher ZnO concentration (200 μg/mL) to investigate whether ZnO nanoparticle uptake could be observed by STXM in the presence of a greater abundance of nanoparticles (Supporting Information, Figure S2). Cell morphology appeared normal at 50 μg/mL ZnO, whereas at 200 μg/mL ZnO all cells developed a spherical morphology.[36] At the lower concentration,
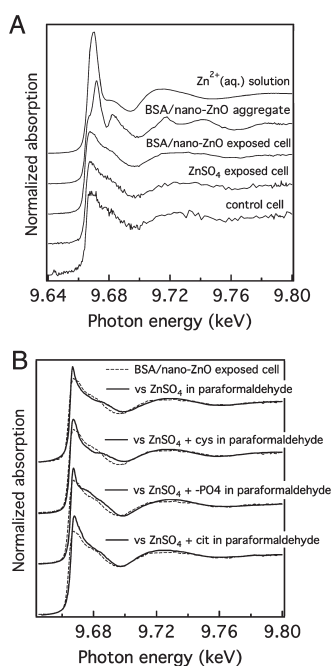
Figure 3. (A) Zinc K-edge X-ray absorption near-edge structure (XANES) spectra from zinc containing reference samples (dissolved Zn^{2+} and BSA-coated ZnO nanoparticles) and from cultured BEAS-2B cells that were either not exposed to zinc (control) or that were exposed to 600 μM ZnSO4 or 50 μg/mL BSA-coated ZnO nanoparticles. No differences in line shape were observed from spectra acquired from other locations within the same cell or between different cells. (B) Comparison of Zn K-edge spectra from intracellular zinc and dried solutions of 1 mM $ZnSO_4$ in 4% paraformaldehyde without (top) or with added coordinating molecules. Cys = cysteine; $-PO_4$ = glucose phosphate; cit = citric acid.

zinc-rich particulates were never detected but at the higher concentration a minority (<10%) of cells had cell-associated ZnO nanoparticles, as observed previously in cell cultures subjected to elevated levels of dissolved zinc or ZnO.[17] However, the identical morphological appearance of cells with and without associated nanoparticles indicates that these particles were not the major cause of toxicity. Thus, even at high zinc concentration, the chemical state and spatial distribution of the zinc responsible for cellular toxicity could not be determined by STXM. All subsequent experiments were performed at 50 μg/mL ZnO.

To further investigate the possible presence of dilute intracellular zinc, we performed X-ray microprobe analysis of the same samples. Micro-XRF elemental mapping of the control sample (Supporting Information, Figure S3) revealed a background concentration of physiological zinc to be just detectable.[26] In addition, all cells exposed to ZnO or to Zn^{2+}(aq) exhibited a substantially higher, diffusely distributed zinc signal (Figure 2). Micro-XRF elemental mapping confirmed that zinc is accumulated within cells following exposure to both nanoparticulate and soluble zinc. The limited spatial resolution precluded the possibility of seeking subcellular areas of zinc accumulation.

X-ray Spectroscopy Study of Intercellular Zinc. To investigate the chemical state of intracellular zinc we collected Zn K-edge XANES spectra from reference materials and from several locations within individual cells. Because the zinc spectra of dissolved and nanoparticulate ZnO are distinct (Figure 3a), this approach has the ability to reveal the presence of nanoparticles in micrometer-scale regions even though the limited spatial resolution precluded direct imaging. The Zn K-edge spectrum of an extracellular aggregate of ZnO nanoparticles exactly matched the reference spectrum of BSA-coated ZnO nanoparticles. The spectra from intracellular zinc from cells in all samples, including the controls, exhibited similar lineshapes that did not match references from BSA-coated ZnO nanoparticles, dissolved Zn^{2+}, or the solid phases $ZnSO_4$ or any zinc hydroxide,[37] nor did they fit any combination of these standards, as confirmed by linear-least-squares fitting.

The lack of sharp structure in the spectra indicates that zinc formed a complex with organic molecules and did not precipitate as a crystalline salt. We additionally acquired spectra from wet and dried samples of 1 mM $ZnSO_4$ in 4% paraformaldehyde to test whether the intracellular zinc was complexed by the fixative molecule. Figure 3b shows that the spectrum of zinc in fixed, dehydrated cells is distinct from the spectrum from the dried $ZnSO_4$/paraformaldehyde sample. Moreover, the spectra of zinc in 4% paraformaldehyde solution and in water are identical. Thus, we find no evidence of zinc binding with paraformaldehyde in fixed cells, consistent with the use of zinc aldehyde in combined fixative and mordant preparations for tissue histology.[38]

Prior Zn K-edge spectra of zinc coordinated with proteins in purified samples and in tissues revealed that the spectral line shape above the X-ray absorption edge varies considerably with the type of organic ligand and the local coordination environment.[39] The spectrum we obtained for intracellular zinc does not match zinc that is tetrahedrally coordinated by four cysteine residues,[40] as is commonly found in zinc-finger motifs. We acquired additional data to test whether the spectrum for intracellular zinc is consistent with zinc complexed by a single functional group (thiol, carboxylic acid, or phosphate groups). Figure 3b shows that none of the spectra from reference solutions dried in the presence of 4% paraformaldehyde provide an exact match to that for intracellular zinc.

Careful comparison of data from control and zinc-exposed cells revealed that the presence of toxic concentrations of zinc from any source led to Zn spectra that were detectably distinct from that obtained from the control sample. We used least-squares linear combination fitting analysis to fit the data from cells with excess intracellular zinc using the spectrum from a control cell and reference spectra (from the present study and the beamline database of zinc standards). The best match was obtained by contributions from the control cell plus one additional thiol ligand
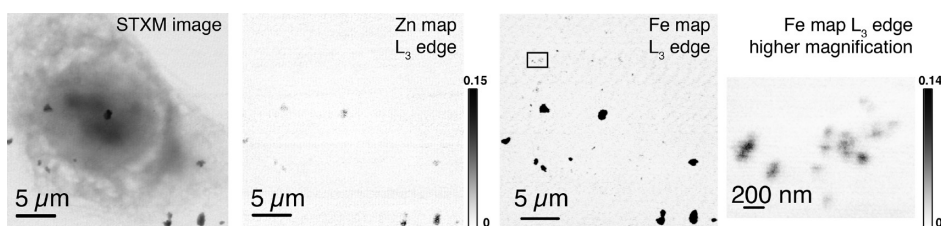
Figure 4. Scanning X-ray transmission microscopy (STXM) image and elemental maps of aggregates of Fe-doped ZnO nanoparticles associated with a BEAS-2B cell. The box in the lower-resolution Fe map indicates the region of detail.
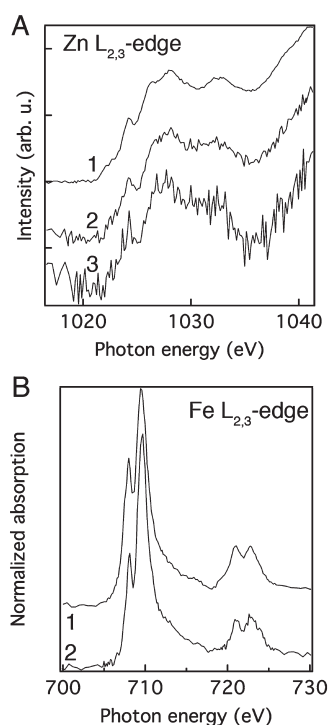

Figure 5. (A) X-ray absorption near-edge structure (XANES) spectra at the Zn $L_{2,3}$ edges of Fe–ZnO doped ZnO nanoparticles. (1) ZnO nanoparticle reference; (2) Fe–ZnO nanoparticle reference; (3) Fe–ZnO nanoparticle aggregate internalized by BEAS-2B cell (spectrum of the internalized aggregate shown in Figure 6). (B) Fe $L_{2,3}$-edges XANES spectra of (1) Fe–ZnO nanoparticle reference; (2) Fe–ZnO nanoparticle aggregate possibly internalized by BEAS-2B cell (spectrum from one iron-rich region in Figure 4).

(Supporting Information, Figure S5). The microprobe data thus provide direct evidence for the accumulation of ionic zinc within cells exposed to ZnO nanoparticles and for the complexation of zinc by organic molecules, and indicate that zinc is ligated by thiol groups. The identity of the biological ligands remain unknown but metallothionein could be a important candidate.

X-ray Spectromicroscopy Studies of Cells Exposed to Fe-Doped ZnO Nanoparticles. The preceding analysis supports the model in which ZnO toxicity is dominated by dissolved Zn^{2+} ions inside cells, but does not resolve whether the intracellular zinc was taken up in the form of aqueous ions or ZnO nanoparticles. To further investigate the cellular interactions and fate of zinc-containing nanoparticles, we exposed BEAS-2B cell cultures to ZnO nanoparticles that

were doped with 10 wt % iron. We previously showed that these Fe–ZnO nanoparticles are significantly less soluble than pure ZnO nanoparticles, as determined by measuring their dissolution rate over a period of 12 h.[18] Although iron addition alters the surface chemistry, as determined by zeta-potential measurements in pure water, both pure and doped nanoparticles exhibit high affinity for adsorption of BSA protein, which dominates their surface properties during cell exposure studies.[18,41,42] BEAS-2B cell cultures were exposed to Fe–ZnO nanoparticles at a concentration of 50 μg/mL using the same procedure and conditions established for undoped materials.

STXM analysis of cell cultures exposed to Fe–ZnO nanoparticles revealed nanoparticle aggregates between 0.1 and 1 μm associated with all cells. As shown in Figure 4, elemental mapping at both Zn and Fe $L_{2,3}$-edges provided identical images of the nanoparticle distribution. As shown in Figure 5, the iron $L_{2,3}$-edge spectra exhibit strong X-ray absorption resonances that represent electronic transitions from 2p to unoccupied 3d states; such strong resonant features are absent in zinc $L_{2,3}$-edge spectra because the 3d states of zinc are fully occupied.[43] The strong resonant features in the Fe $L_{2,3}$-edge, and the increased X-ray absorption at lower energy, permitted higher signal-to-noise element distribution maps to be obtained and smaller nanoparticle aggregates to be revealed (Figure 4). Consequently most nanoparticle distribution mapping was performed at the Fe $L_{2,3}$-edge. STXM analysis of control cultures not exposed to any nanoparticles did not reveal any detectable physiological iron (Supporting Information, Figure S4A–C) except for a single control cell that possessed nanoscale iron-rich regions (Figure S4D). The physiological significance of this observation is uncertain and emphasizes the need for caution during biodistribution mapping of nanomaterials containing physiologically present elements. However, where tested, zinc was found in all cell-associated iron-rich nanoparticles following the addition of Fe–ZnO nanoparticles to BEAS-2B cells. Moreover, the dimensions of the Fe–ZnO nanoparticle aggregates were significantly larger than the dimensions of the iron-rich particles found at one control cell. Thus there is a high degree of confidence that Fe and Zn maps both show the distribution of nonphysiological nanoparticles.

Transition metal $L_{2,3}$-edge XANES spectroscopy is a sensitive probe of structure and metal valence.
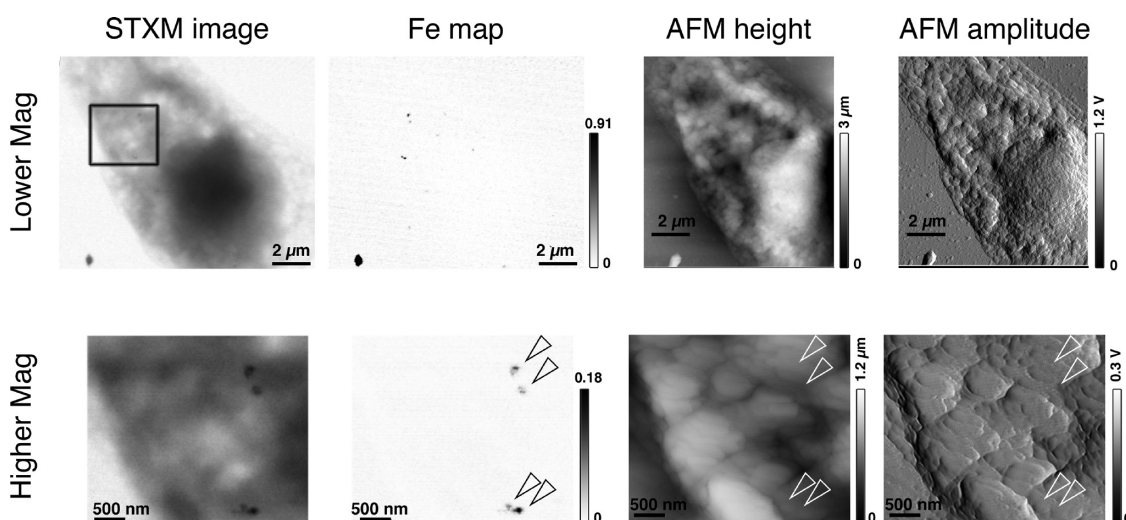
Figure 6. Scanning transmission X-ray microscopy (STXM) and atomic force microscopy (AFM) reveal the presence of internalized Fe-doped ZnO nanoparticles. Each row presents images of the same area at the same magnification; the region of higher-magnification data is indicated by the black box in the top left image. Arrows in the bottom row indicate the locations of iron-rich nanoparticles identified by STXM but absent from the AFM topographical maps.
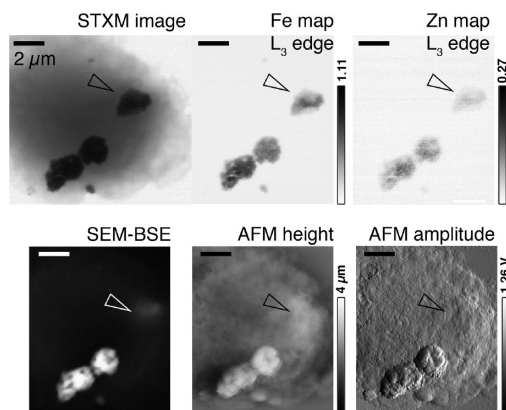

Figure 7. Scanning transmission X-ray microscopy (STXM), atomic force microscopy (AFM), and scanning electron microscopy (SEM) using the backscattered electron (BSE) detection mode reveals the ability of BEAS-2B cells to internalize a very large aggregate of Fe-doped ZnO nanoparticles. The internalized aggregate is indicated by an arrow; larger aggregates remain extracellular. All scale bars represent 2 μm.

Figure 5A compares zinc spectra for bulk ZnO, ZnO nanoparticles, and iron-doped ZnO nanoparticles and reveals an increasing line shape broadening consistent with increasing structural disorder in this sample series previously identified by X-ray diffraction.[18] Within the experimental errors in the zinc spectra acquired from nanoscale aggregates, no structural changes were observed in cell-associated nanoparticles. The energy position and relative intensities of the spectral components at the L_3-edge can be used to quantify ferrous (Fe^{2+}) to ferric (Fe^{3+}) ratios in certain mixed valence materials.[44] The iron spectra of Figure 5B show that, there were no significant changes in the structure or oxidation state of Fe−ZnO nanoparticles following addition to cell culture medium and association with cells.

Complementary STXM and AFM analysis of nanoparticle internalization. The STXM analysis of cell cultures exposed to Fe−ZnO nanoparticles revealed widespread cell−nanoparticle association. However, because STXM is a bulk-sensitive transmission technique, this approach cannot resolve whether cell-associated nanoparticles are intracellular or surface-bound. To address this question, we used atomic force microscopy (AFM) to obtain a topographic description of the cell surface at the nanoparticle locations revealed by STXM. Specific individual cells could easily be identified through comparison of optical, X-ray and AFM micrographs. Sharp topographic images of the fixed cells grown on the Si_3N_4 windows were obtained by tapping-mode AFM analysis, consistent with reported AFM analyses of fixed epithelial cells.[45,46] There was no indication that cellular material or any nanomaterials adhered to the AFM tip and were displaced by it. Future improvement on our sample preparation could follow the method of Francis et al.,[46] (published after our measurements) which showed that cell fixation by 3% glutaraldehyde solution permits superior preservation of cell surface microstructure relative to the 4% paraldehyde solution used by us. Nevertheless, our data quality is sufficient to resolve nanoparticle aggregates whether present on the cell membrane or the Si_3N_4 window.

Figure 6 compares STXM and AFM analyses of one BEAS-2B cell exposed to Fe−ZnO nanoparticles, in which approximately 100-nm aggregates were identified by Fe mapping. The AFM image does not show any topographical features at the location of these aggregates, strongly indicating that they lie beneath the cell membrane. By contrast, a nearby aggregate on the substrate is evident in both STXM and AFM images. Figure 7 provides a striking example of the ability of the cells to internalize large nanoparticle aggregates. In this image, one BEAS-2B cell that has been exposed to three similarly sized (>1 μm) Fe−ZnO nanoparticle

aggregates, is shown. While all three aggregates are clearly mapped in STXM, one aggregate is undetectable by AFM imaging and barely detectable by SEM imaging using the backscattered electron signal, demonstrating that it lies beneath the cell surface.

DISCUSSION

The X-ray microprobe data show that BEAS-2B cells exposed to ZnO nanoparticles accumulate zinc from solution and that only organic-complexed, ionic Zn^{2+} is present intracellularly one hour following exposure. This finding strongly indicates that ZnO toxicity is caused by free or complexed Zn^{2+} within cells, and not by, for example, reactions occurring on the surfaces of internalized solid phase nanoparticles.[47] However, these studies do not reveal whether the uptake of Zn^{2+} or ZnO nanoparticles is the dominant pathway for internalizing zinc. This question was addressed by combined STXM and AFM studies of BEAS-2B cells exposed to less-soluble iron-doped ZnO nanoparticles, which provided evidence that these nanoparticles are readily internalized. Because undoped and iron-doped are not expected to interact differently with cell surfaces when coated by BSA, and because prior abiotic studies showed that undoped ZnO nanoparticles do not completely dissolve under the experimental conditions, we conclude that undoped ZnO nanoparticles encountered and were internalized by the cells. Intracellular dissolution must occur rapidly because no evidence of nanoparticulate ZnO was found during Zn K-edge XANES analysis after one hour of exposure. Cellular uptake of solid-phase ZnO nanoparticles represents a separate pathway for zinc internalization that acts in addition to the uptake of dissolved zinc ions. XANES analysis showed that all intracellular ionic zinc was present in the same chemical form regardless of the uptake route.

CONCLUSIONS AND PERSPECTIVES

Understanding the biological fate and mechanism of toxicity of nanomaterials that are unstable in aqueous solution remains extremely challenging. In this study we used X-ray imaging and spectroscopy to determine the intracellular localization and chemical state of ZnO-based nanomaterials and the metal ion released by ZnO dissolution. X-ray analysis alone was not able to derive a complete model for the mechanism of zinc uptake into nanoparticles. Nevertheless, by combining results from complementary imaging techniques and by comparing the bioaccumulation and toxicity of related nanomaterials (*i.e.,* pure ZnO and lower-solubility Fe-doped ZnO nanoparticles) the present study provided independent corroboration of a model for the cellular toxicity of ZnO that is based on uptake of ZnO nanoparticles followed by intracellular dissolution.

The fields of X-ray imaging and microchemical analyses are undergoing considerable technical evolution that is anticipated to enhance the capability of such methods to contribute to the field of nanotoxicity. More precise quantification of the proportion of solid-phase nanomaterials *versus* soluble transformation products will benefit from the development of approaches for metal detection and speciation that combine high sensitivity and higher spatial resolution. The determination of the subcellular localization of nanomaterials, required for establishing whether uptake has occurred, will benefit from recently commissioned and planned instruments for tomography,[48,49] spectro-tomographic imaging,[50] and cryo-STXM imaging with fluorescence mode X-ray detection with spatial resolution better than 50 nm. Finally, the toxic effect of nanomaterials on cellular physiology is dynamic, and a complete understanding of nanomaterial fate will require observations at multiple time points. Although the high X-ray radiation dose required for X-ray analyses preclude repeated investigations of the internal chemistry of a single living cell,[32] different living cells in a single culture could be studied at multiple time.

MATERIALS AND METHODS

Nanoparticle synthesis. The ZnO or Fe-doped ZnO nanoparticles were prepared using a versatile flame spray pyrolysis method, using the metallorganic precursors, zinc naphthenate (8% of Zn, Strem Chemical, 99.9% pure) or iron naphthenate (12% Fe, Strem Chemical, 99.9% pure). A 50 mL portion of 0.5 M zinc naphthenate was mixed with 6.5 mL of 0.5 M iron naphthenate yielding a 10 mol % Fe content. All precursors were dissolved in an organic solvent (xylene, 99.95%, Strem) to keep the metal concentration at 0.5 M. Each liquid precursor was delivered to the nozzle tip by a syringe pump at a flow rate of 5 mL/min followed by atomizing the precursor solution with dispersant O_2 and maintaining a pressure drop of 1.5 bar. Combustion of the dispersed droplets is initiated by the codelivery of CH_4 and O_2 (1.5 L/min, 3.2 L/min) to create a flame. Titanium dioxide nanoparticles were synthesized and characterized as described previously.[51] Briefly, approximately 6-nm diameter TiO_2 nanoparticles precipitated immediately following the addition of 10 mL of a cold ethanol solution of titanium isopropoxide to 1 L of a rapidly stirred solution pH 1 HCl at 2 °C. The nanoparticles were dialyzed against ultrapure water for 5 days until reaching pH 4, coated with catechol, and dialyzed further to reach pH 7.

Nanoparticle Characterization. The size, crystal phase, crystallinity, and surface areas of dried portions of the nanoparticles were determined using TEM, the Brunauer—Emmett—Teller (BET) gas adsorption method, and X-ray diffraction (XRD) as described in ref 18. A maximum concentration 10% Fe in ZnO was achievable without phase separation, but the crystallite size decreased from 20 nm (no Fe) to 10 nm (10% Fe) with increasing iron concentration. Energy-filtered TEM demonstrated that Fe was homogeneously distributed over the ZnO matrix.

Interactions between metal oxide nanoparticles and the organic and inorganic constituents of cell culture media can influence the surface chemistry and dispersion state of the

nanoparticles and thereby affect their cellular uptake and bioreactivity. Consequently, we performed dynamic light scattering (DLS) and zeta-potential measurements to determine the size and stability of undoped and Fe-doped ZnO nanoparticles in cell culture media containing 2 mg/mL BSA. In the presence of BSA the nanoparticles formed smaller aggregates and exhibited a negative surface charge (in contrast to the positive surface charge observed in pure water), indicating that BSA bound to the nanoparticle surfaces independently of Fe doping concentration.

Cell Culture. Prior to and during the synchrotron measurements, BEAS-2B cells were maintained in type I rat-tail collagen coated flasks using bronchial epithelial growth medium (BEGM; San Diego). The cells were passaged at 70−80% confluence every 2 days. For the nanoparticle exposure studies, cells were grown directly on a 100 nm thick X-ray transparent Si_3N_4 window (Silson Ltd., UK). The window was sterilized by 70% ethanol in water, placed in a well of a 6-well plate, coated with collagen, and rinsed with phosphate buffered saline (PBS). Confluent cells in a flask were detached by trypsin, resuspended in PBS, centrifuged, and transferred to 10−15 mL of growth medium. Approximately 3×10^5 cells were pipetted in sufficient volume of medium to completely cover the window. The cells were grown to 50 − 80% confluence prior to nanoparticle addition and analysis to permit individual cells to be delineated by X-ray microscopy.

Nanoparticle Exposure and Sample Preparation. We used the same conditions for nanoparticle exposure as for prior studies.[17] A portion of the stock nanoparticle suspension was added to 2 mL of BEGM containing 2 mg/mL BSA to make a final concentration of 50 µg/mL ZnO. The solution was placed in a 15 mL Falcon tube, immersed in an ice bath and sonicated for 30 s using a microtip ultrasonic horn (Biologics, Inc., model 150 V/T) at the 50% power setting. The exposure study commenced within 5 min by replacing the initial growth medium with the medium containing the nanoparticles. One higher concentration suspension was prepared at 200 µg/mL ZnO. In a separate experiment, catechol-coated TiO_2 nanoparticles were administered to a cell culture using the same concentration and procedure as for the standard ZnO experiment. The silicon nitride window was removed from the well after 60−90 min.

We developed a vigorous washing procedure to remove nanoparticles and aggregates adhering to cell or substrate surfaces without breaking the fragile 100 nm thick X-ray transparent window. Each sample was held by tweezers, submerged in a pH 4.2 HCl solution for 30 s, and then submerged in a rapidly stirred beaker of deionized water for 1 min. The sample was placed in a solution of 4% paraformaldehyde in phosphate buffered saline for 15 min for fixation then washed for a second time in the beaker of stirred water. The sample was placed in a N_2 purged biosafety cabinet to dry. Prior to all measurements, all samples were inspected with a visible light microscope (VLM) at magnifications up to 50× to verify the absence of ZnO nanoparticle aggregates and to record the locations of specific cells.

Scanning Transmission X-ray Microscopy. We performed scanning transmission X-ray microscopy (STXM) measurements of BEAS-2B cell cultures exposed to zinc oxide (ZnO) and iron-doped ZnO nanoparticles at the Zn and Fe $L_{2,3}$ edges to study the distribution and fate of the nanoparticles and their transformation products. The STXM experiments were conducted at the Molecular Environmental Science beamline 11.0.2 of the Advanced Light Source (ALS) at Lawrence Berkeley National Laboratory.[52] STXM 11.0.2 uses a Fresnel zone plate lens (25 nm outer zones) to focus a monochromatic soft X-ray beam (130−2000 eV) onto a sample that is raster scanned in two dimensions. Transmitted photons are detected with a phosphor scintillator photomultiplier assembly. Image contrast is produced by core electron excitation by X-ray absorption.[53]

X-ray images recorded at energies just below and at the relevant absorption edges (Zn and Fe L_3 −edges) were converted into optical density (OD) images and used to derive elemental maps, with OD = ln (I_0/I), where I_0 is the incident X-ray intensity and I is the transmitted intensity through the sample. Image sequences (i.e., stacks) recorded at energies spanning the Zn $L_{2,3}$ (1010—1045 eV) and Fe $L_{2,3}$ (700—735 eV) absorption

edges were used to obtain XANES spectra from pixel locations of interest. The relative amplitude of the two peaks at the Fe L_3-edge is roughly indicative of the relative proportions of Fe(II) (at 707.8 eV) and Fe(III) (at 709.5 eV) present in the areas of interest. A minimum of two different sample regions were analyzed for each element (Zn and Fe). All measurements were performed at ambient temperature under He at a pressure below 1 atm. The theoretical spatial and spectral resolutions were 30 nm and ±0.1 eV, respectively. The dominant Fe L_3 resonance of a ferrihydrite standard at 709.5 eV was used for relative calibration of the Fe $L_{2,3}$ spectra. The dominant resonance of bulk ZnO set at 1028 eV was used for relative calibration of the Zn $L_{2,3}$ spectra. All data were processed with the aXis2000 software.[54]

X-ray Fluorescence Microprobe. We performed X-ray fluorescence microprobe (µXRF) analysis of BEAS-2B cell cultures (control) and BEAS-2B cell cultures exposed to ZnO nanoparticles to map the association of zinc with the cells and to determine the chemical state of the zinc. Measurements were carried out on beamline 10.3.2 of the ALS[55] following methods fully described in ref 56. Micro-XRF elemental distribution maps were acquired at 11 keV, using a seven-element Ge solid-state detector (Canberra), a beam spot size of 6 µm × 6 µm, a pixel size of 3 µm × 3 µm, and a counting time of 200 ms/pixel. A companion map of an XRF thin film ZnTe mylar calibration standard (Zn: 50.5 µg/cm^2, Micromatter, Canada) was collected at 11 keV using the same incident beam−sample−detector geometry as for the samples to quantify total Zn concentration in the samples. Areas of interest on cells identified by µXRF mapping, and not previously investigated with STXM (to minimize radiation damage), were further investigated by Zn K-edge µXANES. Micro-EXAFS analyses on these samples were precluded due to low Zn counts.

To aid interpretation of the XANES data we prepared 1-mM aqueous solutions of $ZnSO_4$ (Sigma-Aldrich) in ultrapure water and in 10-mM solutions of molecular species possessing functional groups that are potential zinc-coordinating biological ligands: cysteine, citric acid, and glucose phosphate. Zn K-edge XANES spectra were acquired from solutions in sealed glass capillaries with and without 4% paraformaldehyde. Zn spectra were additionally acquired from paraformaldehyde-containing solutions dried onto a zinc-free substrate.

All XANES spectra were collected in fluorescence mode, up to 300 eV above the edge. Spectra were calibrated by setting the Zn foil first derivative to 9660.76 eV,[57] deadtime corrected, pre-edge background subtracted, and postedge normalized using standard procedures.[58] Least-squares linear combination fitting (LCF) of XANES spectra was performed using a library of Zn reference spectra. The best fit was obtained for minimum normalized sum-squares residuals: NSS = 100 × {$\sum(\mu_{exp} - \mu_{fit})^2/\sum(\mu_{exp})^2$} in the 9567−9972 eV range, where μ represents the normalized absorbance. The error on the estimated percentages of species present using this procedure is estimated to ±10%. All data processing and fitting were performed using a suite of custom LabVIEW programs available at the beamline.

Atomic Force Microscopy. We performed atomic force microscopy (AFM) of the BEAS-2B cells on Si_3N_4 windows following STXM and µXRF analyses to determine whether zinc- and iron-rich aggregates identified by STXM analysis were associated with topographic features, and thus determine whether the aggregates were adhering to the cell membrane or had been internalized. AFM was performed in tapping mode using a Digital Instruments MultiMode AFM.

Scanning Electron Microscopy. Scanning electron microscopy was performed with a Hitachi TM1000 at the Electron Microscopy Laboratory at the University of California-Berkeley.

Conflict of Interest: The authors declare no competing financial interest.

REFERENCES AND NOTES

1. Nel, A.; Xia, T.; Mädler, L.; Li, N. Toxic Potential of Materials at the Nanolevel. *Science* **2006**, *311*, 622–627.
2. Nohynek, G. J.; Lademann, J.; Ribaud, C.; Roberts, M. S. Grey Goo on the Skin? Nanotechnology, Cosmetic and Sunscreen Safety. *Crit. Rev. Toxicol.* **2007**, *37*, 251–277.
3. Law, M.; Greene, L. E.; Johnson, J. C.; Saykally, R.; Yang, P. D. Nanowire Dye-Sensitized Solar Cells. *Nat. Mater.* **2005**, *4*, 455–459.
4. Meulenkamp, E. A. Synthesis and Growth of ZnO Nanoparticles. *J. Phys. Chem. B* **1998**, *102*, 5566–5572.
5. Wang, X. D.; Song, J. H.; Wang, Z. L. Nanowire and Nanobelt Arrays of Zinc Oxide from Synthesis to Properties and to Novel Devices. *J. Mater. Chem.* **2007**, *17*, 711–720.
6. Zaveri, T. D.; Dolgova, N. V.; Chu, B. H.; Lee, J. Y.; Wong, J. E.; Lele, T. P.; Ren, F.; Keselowsky, B. G. Contributions of Surface Topography and Cytotoxicity to the Macrophage Response to Zinc Oxide Nanorods. *Biomaterials* **2010**, *31*, 2999–3007.
7. Reddy, K. M.; Feris, K.; Bell, J.; Wingett, D. G.; Hanley, C.; Punnoose, A. Selective Toxicity of Zinc Oxide Nanoparticles to Prokaryotic and Eukaryotic systems. *Appl. Phys. Lett.* **2007**, *90*, 213902.
8. Huang, C.-C.; Aronstam, R. S.; Chen, D.-R.; Huang, Y.-W. Oxidative Stress, Calcium Homeostasis, and Altered Gene Expression in Human Lung Epithelial Cells Exposed to ZnO Nanoparticles. *Toxicol. Vitro* **2010**, *24*, 45–55.
9. Song, W.; Zhang, J.; Guo, J.; Zhang, J.; Ding, F.; Li, L.; Sun, Z. Role of the Dissolved Zinc Ion and Reactive Oxygen species in Cytotoxicity of ZnO Nanoparticles. *Toxicol. Lett.* **2010**, *199*, 389–397.
10. Zhu, X. S.; Zhu, L.; Duan, Z. H.; Qi, R. Q.; Li, Y.; Lang, Y. P. Comparative Toxicity of Several Metal Oxide Nanoparticle Aqueous Suspensions to Zebrafish (*Danio rerio*) Early Developmental Stage. *J. Environ. Sci. Health, Part A* **2008**, *43*, 278–284.
11. Wong, S. W. Y.; Leung, P. T. Y.; Djurisic, A. B.; Leung, K. M. Y. Toxicities of Nano Zinc Oxide to Five Marine Organisms: Influences of Aggregate Size and Ion Solubility. *Anal. Bioanal. Chem.* **2010**, *396*, 609–618.
12. Franklin, N. M.; Rogers, N. J.; Apte, S. C.; Batley, G. E.; Gadd, G. E.; Casey, P. S. Comparative Toxicity of Nanoparticulate ZnO, Bulk ZnO, and ZnCl$_2$ to a Freshwater Microalga (*Pseudokirchneriella subcapitata*): The Importance of Particle Solubility. *Environ. Sci. Technol.* **2007**, *41*, 8484–8490.
13. Wang, H.; Wick, R. L.; Xing, B. S. Toxicity of Nanoparticulate and Bulk ZnO, Al$_2$O$_3$, and TiO$_2$ to the Nematode *Caenorhabtis elegans*. *Environ. Pollut.* **2009**, *157*, 1171–1177.
14. Blinova, I.; Ivask, A.; Heinlaan, M.; Mortimer, M.; Kahru, A. Ecotoxicity of Nanoparticles of CuO and ZnO in Natural Water. *Environ. Pollut.* **2010**, *158*, 41–47.
15. Li, M.; Pokhrel, S.; Jin, X.; Mädler, L.; Damoiseaux, R.; Hoek, E. M. V. Stability, Bioavailability, and Bacterial Toxicity of ZnO and Iron-Doped ZnO Nanoparticles in Aquatic Media. *Environ. Sci. Technol.* **2011**, *45*, 755–761.
16. Fairbairn, E. A.; Keller, A. A.; Mädler, L.; Zhou, D.; Pokhrel, S.; Cherr, G. N. Metal Oxide Nanomaterials in Seawater: Linking Physicochemical Characteristics with Biological Response in Sea Urchin Development. *J. Hazard. Mater.* **2011**, *192*, 1656–1571.
17. Xia, T.; Kovochich, M.; Liong, M.; Mädler, L.; Gilbert, B.; Shi, H. B.; Yeh, J. I.; Zink, J. I.; Nel, A. E. Comparison of the Mechanism of Toxicity of Zinc Oxide and Cerium Oxide Nanoparticles Based on Dissolution and Oxidative Stress Properties. *ACS Nano* **2008**, *2*, 2121–2134.
18. George, S.; Pokhrel, S.; Xia, T.; Gilbert, B.; Ji, Z. X.; Schowalter, M.; Rosenauer, A.; Damoiseaux, R.; Bradley, K. A.; Madler, L.; Nel, A. E. Use of a Rapid Cytotoxicity Screening Approach To Engineer a Safer Zinc Oxide Nanoparticle through Iron Doping. *ACS Nano* **2010**, *4*, 15–29.
19. Brunner, T. J.; Wick, P.; Manser, P.; Spohn, P.; Grass, R. N.; Limbach, L. K.; Bruinink, A.; Stark, W. J. *In Vitro* Cytotoxicity of Oxide Nanoparticles: Comparison to Asbestos, Silica, and the Effect of Particle Solubility. *Environ. Sci. Technol.* **2006**, *40*, 4374–4381.
20. Studer, A. M.; Limbach, L. K.; Van Duc, L.; Krumeich, F.; Athanassiou, E. K.; Gerber, L. C.; Moch, H.; Stark, W. J. Nanoparticle Cytotoxicity Depends on Intracellular Solubility: Comparison of Stabilized Copper Metal and Degradable Copper Oxide Nanoparticles. *Toxicol. Lett.* **2010**, *197*, 169–174.
21. Moos, P. J.; Chung, K.; Woessner, D.; Honeggar, M.; Cutler, N. S.; Veranth, J. M. ZnO Particulate Matter Requires Cell Contact for Toxicity in Human Colon Cancer Cells. *Chem. Res. Toxicol.* **2010**, *23*, 733–739.
22. Yang, Z.; Xie, C. Zn^{2+} Release from Zinc and Zinc Oxide Particles in Simulated Uterine Solution. *Colloids Surf., B* **2006**, *47*, 140–145.
23. Xia, T.; Kovochich, M.; Brant, J.; Hotze, M.; Sempf, J.; Oberley, T.; Sioutas, C.; Yeh, J. I.; Wiesner, M. R.; Nel, A. E. Comparison of the Abilities of Ambient and Manufactured Nanoparticles to Induce Cellular Toxicity According to an Oxidative Stress Paradigm. *Nano Lett.* **2006**, *6*, 1794–1807.
24. Xia, T.; Zhao, Y.; Sager, T.; George, S.; Pokhrel, S.; Li, N.; Schoenfeld, D.; Meng, H.; Lin, S.; Wang, X.; Wang, M.; Ji, Z; Zink, J. I.; Mädler, L.; Castranova, V.; Lin, S.; Nel, A. E. Decreased Dissolution of ZnO by Iron Doping Yields Nanoparticles with Reduced Toxicity in the Rodent Lung and Zebrafish Embryos. *ACS Nano* **2011**, *5*, 1223–1235.
25. Brayner, R.; Ferrari-Iliou, R.; Brivois, N.; Djediat, S.; Benedetti, M. F.; Fievet, F. Toxicological Impact Studies Based on *Escherichia coli* Bacteria in Ultrafine ZnO Nanoparticles Colloidal Medium. *Nano Lett.* **2006**, *6*, 866–870.
26. Podgorczyk, M.; Kwiatek, W. M.; Zajac, W. M.; Dulinska-Litewka, J.; Welter, E.; Grolimund, D. Zinc in Native Tissues and Cultured Cell Lines of Human Prostate Studied by SR-XRF and XANES. *X-ray Spectr.* **2009**, *38*, 557–562.
27. Hernandez-Viezcas, J. A.; Castillo-Michel, H.; Servin, A. D.; Peralta-Videa, J. R.; Gardea-Torresdey, J. L. Spectroscopic Verification of Zinc Absorption and Distribution in the Desert Plant *Prosopis juliflora-valutina* (Velvet Mesquite) Treated with ZnO Nanoparticles. *Chem. Eng. J.* **2011**, *170*, 346–352.
28. Voegelin, A.; Pfister, S.; Scheinost, A. C.; Marcus, M. A.; Kretzschmar, R. Changes in Zinc Speciation in Field Soil after Contamination with Zinc Oxide. *Environ. Sci. Technol.* **2005**, *39*, 6616–6623.
29. Kirz, J.; Jacobsen, C.; Howells, M. Soft-X-ray Microscopes and their Biological Applications. *Q. Rev. Biophys.* **1995**, *28*, 33–130.
30. Pine, J.; Gilbert, J., Live Cell Zpecimens for X-ray Microscopy. In *X-ray Microscopy III*; Michette, A. G., Morrison, G. R., Buckley, C. J., Eds.; Springer-Verlag: Berlin, 1992; Vol. 67, pp 384−387.
31. Williams, S.; Zhang, X.; Jacobsen, C.; Kirz, J.; Lindaas, S.; Vanthof, J.; Lamm, S. S. Measurements of Wet Metaphase Chromosomes in the Scanning-Transmission X-ray Microscope. *J. Microsc. (Oxford, UK)* **1993**, *170*, 155–165.
32. Maser, J.; Osanna, A.; Wang, Y.; Jacobsen, C.; Kirz, J.; Spector, S.; Winn, B.; Tennant, D. Soft X-ray Microscopy with a Cryo Scanning Transmission X-ray Microscope: I. Instrumentation, Imaging and Spectroscopy. *J. Microsc. (Oxford, UK)* **2000**, *197*, 68–79.

33. Graf, C.; Meinke, M.; Gao, Q.; Hadam, S.; Raabe, J.; Sterry, W.; Blume-Peytavi, U.; Lademann, J.; Ruhl, E.; Vogt, A. Qualitative Detection of Single Submicron and Nanoparticles in Human Skin by Scanning Transmission X-ray Microscopy. *J. Biomed. Opt.* **2009**, *14*, 9.

34. Chan, C. S.; De Stasio, G.; Welch, S. A.; Girasole, M.; Frazer, B. H.; Nesterova, M. V.; Fakra, S.; Banfield, J. F. Microbial Polysaccharides Template Assembly of Nanocrystal Fibers. *Science* **2004**, *303*, 1656–1658.

35. Cervini-Silva, J.; Gilbert, B.; Fakra, S.; Friedrich, S.; Banfield, J. Coupled Redox Transformations of Catechol and Cerium at the Surface of a Cerium(III) Phosphate Mineral. *Geochim. Cosmochim. Acta* **2008**, *72*, 2454–2464.

36. Hsiao, I.-L.; Huang, Y.-J. Effects of Various Physicochemical Characteristics on the Toxicities of ZnO and TiO_2 Nanoparticles Toward Human Lung Epithelial Cells. *Sci. Total Environ.* **2011**, *409*, 1219–1228.

37. Waychunas, G. A.; Fuller, C. C.; Davis, J. A.; Rehr, J. J. Surface Complexation and Precipitate Geometry for Aqueous Zn(II) Sorption on Ferrihydrite: II XANES Analysis and Simulation. *Geochim. Cosmochim. Acta* **2003**, *67*, 1031–1043.

38. Mugnaini, E.; Dahl, A.-L. Zinc-Aldehyde Fixation for Light-Microscopic Immunocytochemistry of Nervous Tissues. *J. Histochem. Cytochem.* **1983**, *31*, 1435–1438.

39. Penner-Hahn, J. E. Characterization of "Spectroscopically Quiet" Metals in Biology. *Coord. Chem. Rev.* **2005**, *249*, 161–177.

40. Yu, M.; Yang, F.; Chu, W.; Wang, Y.; Zhao, H.; Gao, B.; Zhao, W.; Sun, J.; Wu, F.; Zhang, X.; Shi, Y.; Wu, Z. 3D Local Structure Around Zn in Kti11p as a Representative $Zn-(Cys)_4$ Motif as Obtained by MXAN. *Biochem. Biophys. Res. Commun.* **2008**, *374*, 28–32.

41. Bihari, P.; Vippola, M.; Schultes, S.; Praetner, M.; Khandoga, A. G.; Reichel, C. A.; Coester, C.; Tuomi, T.; Rehberg, M.; Krombach, F. Optimized Dispersion of Nanoparticles for Biological *in Vitro* and *in Vivo* Studies. *Part. Fibre Toxicol.* **2008**, *5*, 14.

42. Ji, Z. X.; Jin, X.; George, S.; Xia, T.; Suarez, S.; Zhang, H.; Hoek, E. M. V.; Godwin, H.; Nel, A. E.; Zink, J. I. Dispersion and Stability Optimization of TiO_2 Nanoparticles in Cell Culture Media. *Environ. Sci. Technol.* **2010**, *44*, 7309–7314.

43. de Groot, F. M. F. X-ray Absorption Spectroscopy and Dichroism of Transition Metals and Their Compounds. *J. Electron Spectrosc. Relat. Phenom.* **1994**, *67*, 529–622.

44. van Aken, P. A.; Liebsche, B. Quantification of Ferrous/Ferric Ratios in Minerals: New Evaluation Schemes of Fe L-23 Electron Energy-Loss Near-Edge Spectra. *Phys. Chem. Miner.* **2002**, *29*, 188–200.

45. Legrimellec, C.; Lesniewska, E.; Cachia, C.; Schreiber, J. P.; Defornel, F.; Goudonnet, J. P. Imaging the Membrane-Surface of MDCK Cells by Atomic-Force Microscopy. *Biophys. J.* **1994**, *67*, 36–41.

46. Francis, L. W.; Gonzalez, D.; Ryder, T.; Baer, K.; Rees, M.; White, J. O.; Conlan, R. S.; Wright, C. J. Optimized Sample Preparation for High-Resolution AFM Characterization of Fixed Human Cells. *J. Microsc.* **2010**, *240*, 111–121.

47. Nel, A. E.; Mädler, L.; Velegol, D.; Xia, T.; Hoek, E. M. V.; Somasundaran, P.; Klaessig, F.; Castranova, V.; Thompson, M. Understanding Biophysicochemical Interactions at the Nano−Bio Interface. *Nat. Mater.* **2009**, *8*, 543–557.

48. Parkinson, D. Y.; McDermott, G.; Etkin, L. D.; Le Gros, M. A.; Larabell, C. A. Quantitative 3-D Imaging of Eukaryotic Cells using Soft X-ray Tomography. *J. Struct. Biol.* **2008**, *162*, 380–386.

49. Dierolf, M.; Menzel, A.; Thibault, P.; Schneider, P.; Kewish, C. M.; Wepf, R.; Bunk, O.; Pfeiffer, F. Ptychographic X-ray Computed Tomography at the Nanoscale. *Nature* **2010**, *467*, 436–439.

50. Obst, M.; Wang, J.; Hitchcock, A. P. Soft X-ray Spectro-tomography Study of Cyanobacterial Biomineral Nucleation. *Geobiology* **2009**, *7*, 577–591.

51. Finnegan, M. P.; Zhang, H.-Z.; B., J. F. Phase Stability and Transformation in Titania Nanoparticles in Aqueous Solutions Dominated by Surface Energy. *J. Phys. Chem. C* **2007**, *111*, 1962–1968.

52. Tyliszczak, T.; Warwick, T.; Kilcoyne, A. L. D.; Fakra, S.; Shuh, D. K.; Yoon, T. H.; Brown, G. E., Jr.; Andrews, S.; Chembrolu, V.; Strachan, J.; Acremann, Y. Soft X-ray Scanning Transmission Microscope Working in an Extended Energy Range at the Advanced Light Source. *AIP Conf. Proc.* **2004**, *705*, 1356–1359.

53. Stöhr, J. *NEXAFS Spectroscopy*; Springer-Verlag: Berlin, 1992.

54. Hitchcock, A. P. aXis-2000 is an IDL-based analytical package. 2000, http://unicorn.mcmaster.ca/aXis2000.html.

55. Marcus, M. A.; MacDowell, A. A.; Celestre, R.; Manceau, A.; Miller, T.; Padmore, H. A.; Sublett, R. Beamline 10.3.2 at ALS: a Hard X-ray Microprobe for Environmental and Materials Sciences. *J. Synchrotron Radiat.* **2004**, *11*, 239–247.

56. Manceau, A.; Marcus, M. A.; Tamura, N. Quantitative Speciation of Heavy Metals in Soils and Sediments by Synchrotron X-ray Techniques. In *Reviews in Mineralogy and Geochemistry*; Applications of Synchrotron Radiation in Low-Temperature Geochemistry and Environmental Science; Mineralogical Society of America: Washington, DC, 2002; Vol. 49, pp 341−428.

57. Kraft, S.; Stümpel, J.; Kuetgens, U. High Resolution X-ray Absorption Spectroscopy with Absolute Energy Calibration for the Determination of Absorption Edge Energies. *Rev. Sci. Instrum.* **1996**, *67*, 681–688.

58. Kelly, S, H., D., Ravel, B, Analysis of Soils and Minerals using X-ray Absorption Spectroscopy. In *Methods of Soil Analysis, Part 5—Mineralogical Methods*; Ulery, A. L., Drees, L. R., Eds.; Soil Science Society of America: Madison, WI, 2008; pp 367−464.